Applied Surface Science 730 (2026) 166200

Contents lists available at ScienceDirect

Applied Surface Science

journal homepage: www.elsevier.com/locate/apsusc

Full Length Article

Strain tailoring in heavily Sb-doped Ge via pulsed laser melting

Francesco Sgarbossa [a,b,*], Davide Valzani [a,b], Filippo Nicolasi [a,b], Gianluigi Maggioni [a,b], Chiara Carraro [a], Marco Romagnoni [c,d], Thu Nhi Tran Caliste [e], John P. Sutter [f], Enrico Napolitani [a,b], Davide De Salvador [a,b,*]

[a] Department of Physics and Astronomy, Università degli Studi di Padova, Via Marzolo n. 8, 35131 Padova, Italy
[b] Istituto Nazionale di Fisica Nucleare, Laboratori Nazionali di Legnaro, Viale dell'Università n. 2, 35020 Legnaro, (PD), Italy
[c] Department of Physics and Earth Sciences, Università degli Studi di Ferrara, Via Giuseppe Saragat 1, 44121 Ferrara, Italy
[d] Istituto Nazionale di Fisica Nucleare, Sezione di Ferrara, Via Giuseppe Saragat 1, 44121 Ferrara, Italy
[e] European Synchrotron Radiation Facility, Grenoble, France
[f] Diamond Light Source, Didcot, United Kingdom

ARTICLE INFO

Keywords:
Antimony
Germanium
Doping
Bent crystals
Channeling

ABSTRACT

This study investigates the lattice strain induced by Ge:Sb alloy films on Ge substrates. Metastable films are formed by UV pulsed laser melting (PLM) of a Sb-coated Ge substrate. We fabricate thin Ge:Sb layers, systematically varying processing parameters and crystal orientation to study strain and strain-relaxation-induced defects. High-resolution X-Ray diffraction and electrical characterization revealed extremely high strain values as well as ultra-low resistivity induced by Sb. Maximum strain before the onset of strain relaxation was found to depend on crystal orientation with the Ge (111) orientation yielding the highest strain values. By combining structural as well as electrical information, we estimated Sb contribution to lattice expansion, separating electronically active from inactive fractions. Strain optimization was applied to an innovative application that is the production of bent crystals for high energy particle beam deflection and radiation production. Bending tests on thin Ge substrates confirmed the method, with controlled PLM processing allowing inducing quantifiable curvature with smallest achievable radii of 4.5 m. Exploiting non-equilibrium doping/alloying to exceed equilibrium Sb solubility is promising for applications ranging from ultra-low-resistivity layers in scaled nano-electronic devices to bent crystals for advanced systems like crystal-based undulators, enabling new approaches to high-energy photon production.

1. Introduction

Germanium crystals are currently a widely used material in cutting-edge scientific research for applications ranging from gamma [1–3] and IR sensing [4–7] to medical imaging applications [8] and uses in micro-nanoelectronics [9] as well as photonics [10], and for applications in accelerated beam physics [11–14]. Common features among these applications are the availability of germanium crystals with excellent crystalline quality, i.e. a very low or negligible concentration of lattice defects, high control of doping impurities from high purity germanium bulk material to hyper doped germanium films [3,15,16], and high control of lattice strain.

In the development of Ge-based devices, crystal lattice strain is a fundamental parameter that directly influences the intrinsic properties of germanium, such as its band structure [17–19]. Strain can be introduced by stressor layers or through direct mechanical deformation. In micro- and nano-electronic applications, epitaxial layers of alloys or highly doped crystals can induce strain and modify electronic properties. For example, Ge:Sn alloys [20,21] have attracted significant interest in recent studies [18,22–24], as well as for emerging quantum technologies, such as the realization of germanium-based qubits [25] for quantum computing [26,27]. Furthermore, lattice strain can be harnessed to produce bent crystals, which are crucial in experiments involving the coherent interaction of accelerated beams with crystals [28–33].

Pulsed laser melting (PLM) has yielded promising results in the formation of alloyed films, as it enables the synthesis of highly concentrated alloys and doped layers. This advantage arises from its non-equilibrium processing conditions, which allow surpassing the solubility limits of alloying and doping elements [15,16,34,35]. This is

* Corresponding authors at: Department of Physics and Astronomy, Università degli Studi di Padova, Via Marzolo n. 8, 35131 Padova, Italy.
E-mail addresses: francesco.sgarbossa@unipd.it (F. Sgarbossa), davide.desalvador@unipd.it (D.D. Salvador).

https://doi.org/10.1016/j.apsusc.2026.166200
Received 18 November 2025; Received in revised form 23 January 2026; Accepted 2 February 2026
Available online 12 February 2026

particularly relevant for several applications, such as ultra-low resistivity layers for nanoelectronics, hyper-doped layers for photonic and plasmonic applications in the NIR range with low plasma wavelength, etc. Furthermore, a highly promising new application of this research explored in this paper lies in the fabrication of curved crystals for high-energy beam manipulation [11]. As widely reported in the literature, single curved crystals can bend particle beams ranging from a few MeV up to ultra-relativistic energies through the channeling effect. These crystals are increasingly recognized as promising candidates for advanced beam optics in next-generation accelerators [36] and for the generation of high-energy electromagnetic radiation [13,37].

Exploiting the ability to deflect beam trajectories using only the electrostatic potential of the crystal, thus avoiding the need for superconducting magnets operating at extremely high fields, curved crystals can enable the production of electromagnetic radiation from energetic beams that surpasses the limits imposed by current magnet, and undulator-based technologies [13,37,38]. At the forefront of current research is the development of crystal undulators with periods on the order of hundreds of microns, which could enable radiation generation at energies equal to or exceeding the MeV scale [39]. This would be achieved by imposing a periodic sinusoidal deformation in a bent single crystal, thereby inducing undulation in an ultra-relativistic particle beam [40,41].

In the case of germanium employed for coherent interaction with accelerator beams, sample deformation induced by strain is most often applied at the macroscopic scale through mechanical methods, such as anticlastic or quasi-mosaic bending. While for silicon several approaches have been proposed that exploit stress-inducing films to deform the crystalline lattice [42–44], only limited effort has been directed toward germanium, despite its potential advantages for beam interaction efficiency arising from its higher atomic mass [45,46].

Over the past decades, considerable research has focused on the development of crystalline undulators [37,39,47–50], devices designed to generate high-brilliance radiation when a periodically deformed lattice is traversed by an accelerated beam. In this case, pure mechanical bending is not a feasible solution, and surface stressor layers suitable for micro-patterning are required. To date, however, such approaches have been proposed almost exclusively for silicon [42,48].

Beyond accelerator-beam applications, strain engineering in Ge is also highly relevant to Si-integrated platforms, particularly Ge-on-Si and Ge-on-insulator (GOI), including SOI-based architectures, where high crystalline quality is pursued for electronic and photonic devices [51]. In parallel, Ge-on-Si and GOI platforms have enabled key device concepts such as Ge-on-Si photodetectors and Ge waveguides on GOI wafers, as well as local Ge-on-insulator structures where strain is used to tailor the electronic band structure [51].

In this context, the stressor-layer approach investigated here namely, PLM-enabled formation of epitaxial Ge:Sb layers with large, controllable strain, can be viewed as a potentially transferable building block for Si-compatible Ge stacks, while recognizing that Ge-on-Si/GOI structures may include pre-existing epitaxial/thermal strain and interface-related defect distributions that must be accounted for in future integration studies.

The aim of this work is to establish a foundation for bridging micro- and nano-electronic pulsed laser melting processing (used to produce thin-film alloys) with the fabrication of crystalline devices for accelerated beam applications. Specifically, we investigate the limits of strain deformation that can be achieved by Sb incorporation in Ge through PLM. Previous studies have shown that Sb can be very efficiently introduced into the Ge lattice via PLM, reaching both very high doping levels and strain values [16,52]. Notably, the lattice expansion induced by Sb is larger than that induced by Sn, even though Sb and Sn atoms have comparable atomic dimensions. In fact, according to the expression $a_{Ge:dopant} = a_{Ge} + \Delta a_{dopant} x$ which relates the lattice parameter $a_{Ge:dopant}$ to the dopant atomic concentration x, the specific expansion for Sn $\Delta a_{Sn} =$ 0.8 Å [21] increases up to about Δa_{Sb} ~1.7 Å [16,53,54] for Sb. This difference arises from the electronic contribution associated with the dopant nature of Sb [55]. These characteristics make Sb alloying/doping a highly promising route for strain engineering in Ge.

Despite this understanding, the maximum strain achievable through Sb alloying/doping using PLM remains unclear, and no studies have addressed so far the feasibility of employing different substrate orientations, as required for advanced beam devices. In this work, we perform a systematic investigation by varying the laser energy density, number of pulses, Sb precursor film thickness, and crystallographic orientation of Ge substrates. For each set of process parameters, both the absence of strain relaxation defects and the strain profile, i.e. the strain deformation ($\epsilon_{\parallel} = (a_{Ge} - a_{Ge:Sb})/a_{Ge:Sb}$) as a function of the depth of the PLM-processed layer, are evaluated. High-Resolution X-Ray diffraction (HRXRD) is employed, enabling precise determination of the onset of strain relaxation and the maximum strain deformation attainable in the layer. A further unresolved aspect of the PLM Ge:Sb process concerns the role of non-active Sb. Not all Sb atoms contribute electrons to the conduction band, and the structural nature as well as the strain contribution of these electrically inactive Sb atoms remain to be clarified. Bearing in mind the potential applications that involve inducing bending in the bulk, we also evaluated in specific samples the curvature induced by the homogeneous film into the substrate.

Stoney's formula [56] relates the substrate radius of curvature R to the mechanical properties of the stressor layer acting on it:

$$\sigma_f t_f = \frac{E_s h^2}{6(1-\nu_s)} \frac{1}{R} \tag{1}$$

where $\sigma_f t_f$ is the product of the in-plane stress component and the film thickness [57], E_s is the Young's modulus of the substrate, h is the thickness of the substrate and ν_s is the Poisson ratio of the substrate.

When the lattice constants of the film are equal (or can be approximated as equal) to those of the substrate, as in the case of Ge:Sb alloys, Eq. (1) can be simplified to:

$$\epsilon_{\parallel} t_f = \frac{h^2}{6} \frac{1}{R} \tag{2}$$

where $\epsilon_{\parallel}$ is the strain parallel component. We note that, while in the first case the curvature may change when different crystal directions are considered, due to the anisotropy of the elastic constant characteristic of a crystalline substrate, in the second case the elastic constants of the film and the substrate are the same in every direction and simplify to yield a single curvature in all directions.

Eq. (2) can be further generalized for the case of a non-homogeneous strain distribution along the film thickness:

$$\int_0^{t_f} \epsilon_{\parallel}(t) dt = \frac{h^2}{6} \frac{1}{R} \tag{3}$$

Thus, the radius of curvature R can be directly related to the strain profile of the film, given the film and substrate thicknesses, parameters that can be experimentally measured. The strain integral measured by HRXRD, $\int_0^{t_f} \epsilon_{\parallel}(t) dt$ is successfully compared with the experimentally measured curvature radius R of selected samples, validating this approach. The strain integral is then employed as an optimization parameter to guide the selection of PLM processing conditions that yield high lattice deformation.

2. Experimental

2.1. Sample preparation

A double polished undoped Ge ((1 1 1), (1 1 0) and (0 0 1)) wafer (supplied by Biotain) was cut in 0.9 × 0.8 cm^2 samples and cleaned with hot 2-propanol, acetone and bi-distillate water to remove dicing residuals. Two types of sample thicknesses were produced: 0.5 mm-thick

samples were primarily used for the diffraction and electrical activation studies, while thinner samples, with thicknesses ranging from 150 to 180 μm, were specifically fabricated for the bending tests.

Sb deposition on Ge substrates was conducted via RF magnetron sputtering: the germanium substrates were placed in a stainless-steel vacuum chamber, evacuated to a base pressure lower than 1×10^{-4} Pa, and by a RF magnetron sputtering equipment (power set at 30 W), different thicknesses of metallic Sb (99.9999% purity supplied by ACI Alloys) were deposited on the substrates. The sputtering deposition rates, and the final Sb thickness were determined via RBS analysis [58].

2.2. Diffusion process via non-equilibrium technique

The deposited Sb layers were thermally processed by using Pulsed Laser Melting (PLM) to promote the metal in-diffusion into Ge substrate and forming the desired superficial stressor layer. A KrF laser (Coherent COMPex 201F) with a single pulse of 22 ns, delivering a wavelength equal to 248 nm was used for this scope, allowing the melting of the sample surface in a 5×5 mm^2 spot of the laser. The laser energy density and the number of pulses used in the treatments were varied in a range from 400–900 mJ cm^{-2} and 1–32 pulses (1 Hz repetition rate). The resulting lateral resolution at the sample plane is <30 μm thanks to the installed optical path. These parameters guaranteed that the Ge surface was melted and the Sb diffused toward the bulk with no Sb loss [16]. After a thermal dissipation delay (around 100–200 ns, depending on laser parameters [59–61]) the Ge epitaxially regrew and the Sb diffused in liquid Ge was incorporated in the crystal lattice. The resulting layers were epitaxial to the substrate and generally exhibited excellent crystallographic quality, as already highlighted by several studies in the literature [16,34]. The laser process was performed at room temperature, in a low dust environment.

2.3. Characterization techniques

High Resolution X-Ray diffraction (HRXRD) was used to analyse the strain status and the presence of defects of Ge:Sb thin films by collecting reciprocal space maps and/or high-resolution scans. Omega-2theta scans were collected for assessing the film strain status through an X-Ray scattering simulation software called AMASS (Advanced Material Analysis and Simulation Software by Panalytical), while high resolution Omega scan was performed along film peak to monitor the presence of defects. Strain profile was modelled by a linear spline with 4 knots mimic with enough accuracy the diffusion profile and optimized minimizing the agreement between data and simulation by Genetic Algorithm embedded in the analysis software. All these measurements were performed using a Panalytical MRD X'Pert Pro diffractometer mapping different symmetrical and asymmetrical reflections depending on the substrate crystallographic orientation. The system was equipped with a Cu anode source, a W/Si multilayer parabolic mirror, and a Bartels 4-bounce Ge (2 2 0) asymmetric monochromator. Specifically, Kα1 radiation (8 keV) was chosen as the probing beam, and the angular acceptance was limited to 12 arcseconds by a detector with a channel-cut (2 2 0) analyser. Overall resolution (divergence plus acceptance) of about 18 arcsec was obtained in the used set-up.

The electrical characterizations were conducted with a four-probe electrical apparatus according to the Van der Pauw method. The setup, provided by MMR Technologies, included a vacuum chamber housing four gold probes, which were connected to a Keithley 2600 source-meter and a switch matrix. This configuration enabled sheet resistance and Hall effect measurements to determine carrier concentration. The entire system was operated via custom-developed software. For Hall measurements, a 0.65 T permanent magnet was integrated into the system [62]. The analysis of the electrical measurements was carried out in accordance with the literature and our previous work [16,53]. The starting Ge wafers are nominally undoped (about 2×10^{13}cm^{-3}); the corresponding substrate areal carrier density (~1×10^{12} cm^{-2} for a 0.5 mm wafer) is ≪1% of the minimum Hall doses reported here, hence the substrate contribution is negligible.

A Tencor Profilometer P17 was used to measure the radius of curvature of sample by measuring the bow of sample surface before and after the stressor thin film synthesis. This measurement was made possible using a custom-designed sample holder that ensures reproducible sample mounting. The holder unique feature was its three-sphere support system, which guaranteed that the sample rested on only three points, thereby minimizing potential distortions and ensuring consistent positioning across multiple measurements.

The antimony layers on Ge were characterized by Rutherford Backscattering Spectrometry (RBS) before and after the laser treatment by using $^4He^+$ beam at 2.0 MeV delivered by AN2000 accelerator at INFN Laboratori Nazionali di Legnaro. Random and channeling measurements were used to perform a quantitative analysis of the thickness and to perform lattice localization measurements, respectively. Energy and solid angle calibrations were performed by using standard samples and the scattering angle for all measurements were set to 160° [63]. To enable channeling alignments and angular scans, a five-axis goniometer was used: the various samples were mounted on it, and their positioning was performed with an accuracy better than 0.01°.

Atomic force microscopy (AFM) topography maps were acquired in ambient conditions on selected samples to assess the post-PLM surface morphology and correlate it with the structural response of the Ge:Sb stressor layer. A Nanosurf Flex AFM was used in tapping mode, mapping 5×5 or 2×2 μm^2 areas inside PLM laser spots using PPP tips.

Atomic force microscopy was also operated in Kelvin Probe Force Microscopy (KPFM) mode by exploiting a second lock-in amplifier available in our setup, using dedicated conductive probes (Multi75E-G) and grounding the sample. In this configuration, we simultaneously acquired the sample topography and the tip-voltage (surface potential) maps, which, depending on the specific KPFM implementation, provide spatially resolved information related to local work-function variations. The voltage maps were not calibrated; therefore, the measured tip-voltage must be interpreted only as relative contrast, rather than as an absolute work-function value.

Finally, Synchrotron X-Ray topography was carried out to analyze the bent samples of selected Ge crystals. Rocking Curve Imaging [64] (RCI) offering high spatial (~6 μm) and angular (μrad) resolution were acquired using monochromatic 10.5 KeV X-Ray at the Diamond Light Source synchrotron (beamline B16) [65]. It involved capturing around 300 diffraction images at different ω angles across the Bragg peak using a high-resolution 2D detector in Laue conditions. The variation in intensity of each pixel formed a rocking curve, which was analyzed individually through dedicated software. The RCI analysis software, which has been developed at BM05 beamline at ESRF, was used to fit each pixel of each RC by using a Gaussian function. This produces the values of integrated intensity, FWHM and peak position of each pixel. Among the various pieces of information that can be extracted, the shift in the diffraction peak position as a function of position (image pixels) provides information on the bending of the sample.

3. Results and discussion

A large set of samples, synthesized by Sb sputtering deposition on Ge substrate followed by PLM treatment (see the experimental section) has been analyzed using various techniques to quantitatively assess the effectiveness of employing a thin Ge:Sb layer as a stressor to induce crystal bending. To achieve this, a wide range of process parameters has been explored to evaluate the influence of as many variables as possible. The most critical parameters investigated include the laser energy density, the number of laser pulses, the initial antimony areal density, and the crystallographic orientation of the germanium substrate.

3.1. The strain status of stressor films

The most important analysis to verify the state of the Ge:Sb stressor layer is through HRXRD, which can provide us with various information regarding the strain state and defect structure of the material.

Fig. 1a shows the asymmetrical reciprocal space mapping of Ge (1 1 0) sample with 7.5 × 10^{15}cm^{-2} Sb and treated with 500 mJ cm^{-2} with 2 laser pulses. The map presents two distinguishable main peaks, one from the Ge substrate (placed at origin of the map, i.e. ΔQz = Qz – Qz^{Ge444} = 0) and the other from the film (placed at about ΔQz −0.023), connected by a rod. They have the same $Q_{\parallel}$ (or $Q_{x,y}$), indicating that the substrate and the film have exactly same in plane lattice size. The germanium substrate has a cubic symmetry while the Ge:Sb film shows a tetragonal deformation pseudomorphic to the substrate. Moreover, there are no significant intensity broadenings either around the substrate or around the film, confirming that the laser treatment did not induce extended defects in the sample. This indicates that the sample under analysis (Ge (1 1 0) presenting a 7.5 × 10^{15} cm^{-2} Sb and treated with 500 mJ cm^{-2} with 2 laser pulses) exhibits a pseudomorphic layer with respect to the substrate without any sign of layer relaxation.

In contrast, Fig. 1b, reporting the HRXRD collected in a sample with higher Sb areal density and treated with higher number of pulses, also shows two distinguishable peaks, but a clear lateral broadening of the film peak indicates a significant presence of defects in the film and is indicative of partial relaxation. The latter is confirmed by the intensity tail that begins to form towards the left part of the image, suggesting a partial relaxation of a small part of the volume from a tetragonal back to a cubic structure with bigger lattice parameter (remembering that smaller Q values correspond to bigger direct lattice dimensions). It is also useful to note that despite the sample having a higher quantity of Sb (2.5 × 10^{16} cm^{-2} instead of 7.5 × 10^{15} cm^{-2}), the film peak is positioned at lower $Q_{\perp}$ (or Q_z) values, indicating less strain induced by the partially relaxed film.

To save analysis time, the presence of relaxation is quickly monitored in all the produced samples by single horizontal scans along the film peak, looking for the width of the rod that corresponds to the HRXRD resolution in case of non-detectable relaxation (Fig. 1a) and is instead broader in case of relaxation (Fig. 1b).

The omega-2theta scans of defect-free films were then analyzed using strain simulation software as described in the previous section, yielding a strain profile as a function of depth. An example of this analysis is shown in Fig. 2a and b, where data and the best fitting are compared. Thanks to this analysis, the strain profile of the synthesized film is given as an output of fitting (Fig. 2c and d) and thus the maximum strain and the strain integral can be easily estimated. Strain integral constitutes a key parameter since, by means of Stoney's equation Eqs. (2) & (3), it enables the analytical determination of the radius of curvature of a sample bearing such a homogeneous film.

A collection of all the integrals of strain obtained from HRXRD measures is shown in Fig. 3, rationalized by the amount of antimony present (varying from column to column), the crystallographic direction of the Ge substrate (varying from row to row), and then each graph represents the strain integral as the laser parameters vary, namely the energy density and the number of laser pulses. If the sample shows the presence of defects in the film, it will be indicated with an orange dot, signifying the onset of the relaxation phenomenon. If not, the blue circle radius is instead proportional to the strain integral.

At first glance, Fig. 3 shows a rather complex scenario, where the film deposited behaves differently depending on various parameters used. In particular, the quantity of deposited Sb is the first important parameter which modifies the amount of strain within the material due to the quantity of dopant present: as one would naturally expect, higher doses of antimony lead to a general increase in strain, given the same process conditions. This effect is particularly pronounced along the (1 1 1) and (1 0 0) directions, whereas in the (1 1 0) direction relaxation mechanisms are activated at an earlier stage, preventing a clear observation of this trend.

The energy density and number of laser pulses also modify the strain integral, acting on the incorporation of the dopant, that is, on the diffusion within the material and the complex dynamics of melting and the epitaxial regrowth [34,52]. High energy densities will result in a thicker melted layer and thus deeper diffusion, but at the same time, a higher thermal budget and longer lifetime of the liquid phase. The number of successive pulses (1 Hz repetition rate) also primarily affects the diffusion of the dopant, promoting its diffusion in the liquid phase and thus widening and flattening the dopant diffusion profiles as a function of depth. A high number of pulses can also cause an increase in the maximum melt depth, a phenomenon already observed in previous

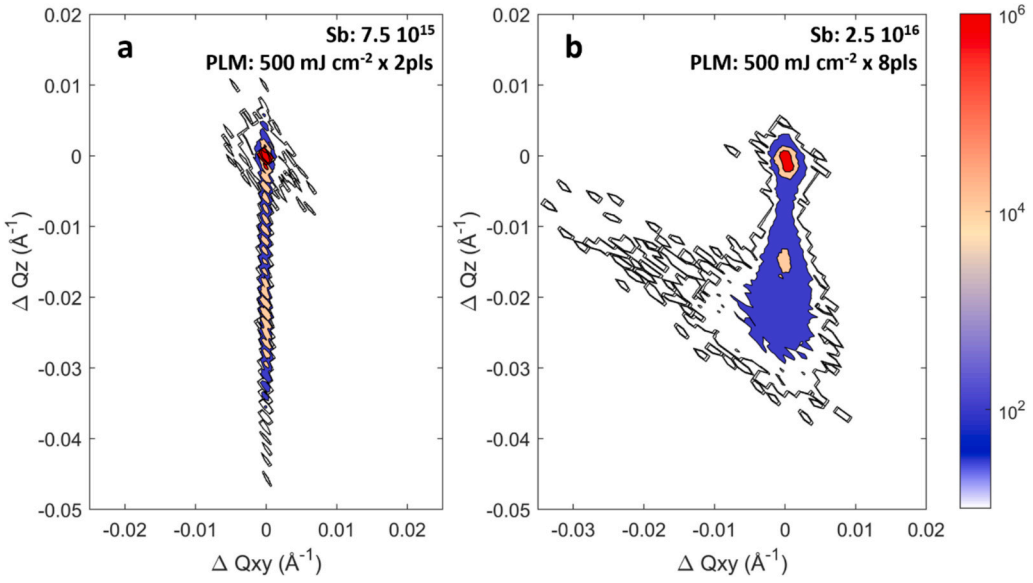

Fig. 1. Two examples of Ge (444) reciprocal space maps on Sb in Ge film produced by PLM: (a) asymmetrical reciprocal space mapping of Ge (110) sample presenting a 7.5 10^{15}cm^{-2} Sb and treated with 500 mJ cm^{-2} with 2 laser pulses is shown. (b) Asymmetrical reciprocal space mapping of Ge (110) sample presenting a 2.5 10^{16}cm^{-2} Sb and treated with 500 mJ cm^{-2} with 8 laser pulses. Both maps are expressed in reciprocal space units Q with the origin shifted in the Ge substrate peak.

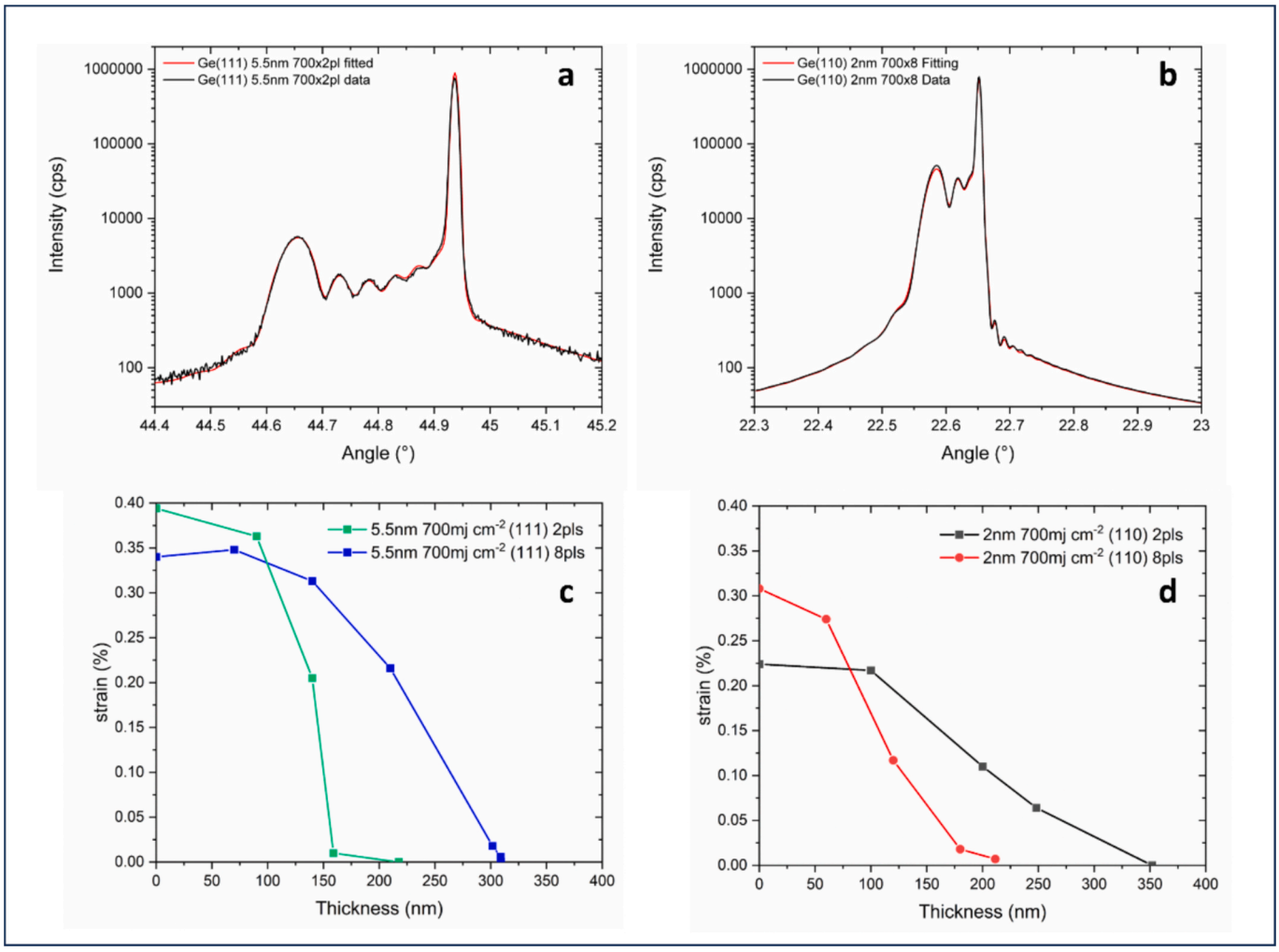

Fig. 2. HRXRD omega-2theta scans along rod and data analysis. a) Ge (111) 5.5 nm 700 mJ cm^{-2} 2 pls rocking curve (black data) and its best fitting in red. b) Ge (110) 2 nm 700 mJ cm^{-2} 8 pls sample rocking curve (black data) and their best fitting in red. The best fit results are shown as a strain profile as a function of the sample depth for c) Ge (111) 5.5 nm 700 mJ cm^{-2} 2pls and 8 pls and d) Ge (110) 2.0 nm 700 mJ cm^{-2} 2 pls and 8 pls. (For interpretation of the references to colour in this figure legend, the reader is referred to the web version of this article.)

works on Ge:Sb PLM systems [16,52].

The onset of the film relaxation phenomenon in these systems is not trivial, given that the system is out of thermodynamic equilibrium, and the formed layers present an amount of Sb in Ge that is higher than the equilibrium solid solubility (equal to 1.2×10^{19} cm^{-3}) [66].

The first dependency that appears is the different behavior observed between various crystallographic directions. In particular, the (1 1 0) direction shows layer relaxation under milder conditions compared to the (1 0 0) and (1 1 1) directions. Since defects appears to be insensitive to the crystal symmetry in these systems [21,67], this different behavior can be attributed to different interfacial undercooling temperatures during epitaxial regrowth, as suggested by the literature [68]. Specifically, a different interfacial undercooling between the (1 0 0) and (1 1 1) directions of Ge has been demonstrated with the use of a KrF laser, which would cause a different liquid/solid interface temperature, lowering the thermal budget for defect formation, thus giving rise to a different rate of defect formation depending on the crystallographic direction. More in detail, time-resolved X-Ray diffraction experiments on Ge under KrF pulsed-laser melting measured a pronounced orientation-dependent kinetic undercooling, with regrowth on (1 1 1) requiring substantially larger undercooling than (0 0 1) and exhibiting a distinct velocity–temperature response in the undercooling regime. This implies that regrowth kinetics depend strongly on orientation under PLM conditions. In our system, a larger undercooling would translate into a lower effective interface temperature during regrowth for comparable velocities, plausibly reducing the thermal budget available for defect evolution and delaying the onset of strain relaxation. A quantitative treatment for all orientations would require dedicated in-situ time-resolved measurements and is beyond the scope of the present work.

A second parameter influencing the layer relaxation is given by the amount of Sb in the layer. As the number of Sb atoms increases, the misfit between the layer and the bulk consequently increases, and therefore it is entirely reasonable to expect that relaxation phenomena may occur as the Sb dose increases. However, the total Sb dose is distributed in the layer differently, depending on the laser treatment, and thus the relaxation also depends on the energy density used and the number of pulses. Indeed, the diffusion profile of the dopant in the layer is not box-like, but follows the laws of diffusion in liquid, forming the typical PLM diffusion profiles well known in the literature [34,69]. The higher the laser energy density, the greater the thermal budget to which the system is subjected, increasing the probability of defect formation and layer relaxation. The number of pulses can act in two ways: at a high number of pulses, the dopant redistributes throughout the entire melted thickness, decreasing its maximum concentration and thus potentially giving rise to a relaxation recovery phenomenon, as can be seen from the series 400 mJ cm^{-2} Ge (1 1 0) 3.5 nm and with 4 and 8 pulses. Conversely, it may happen that with an increasing number of pulses, the

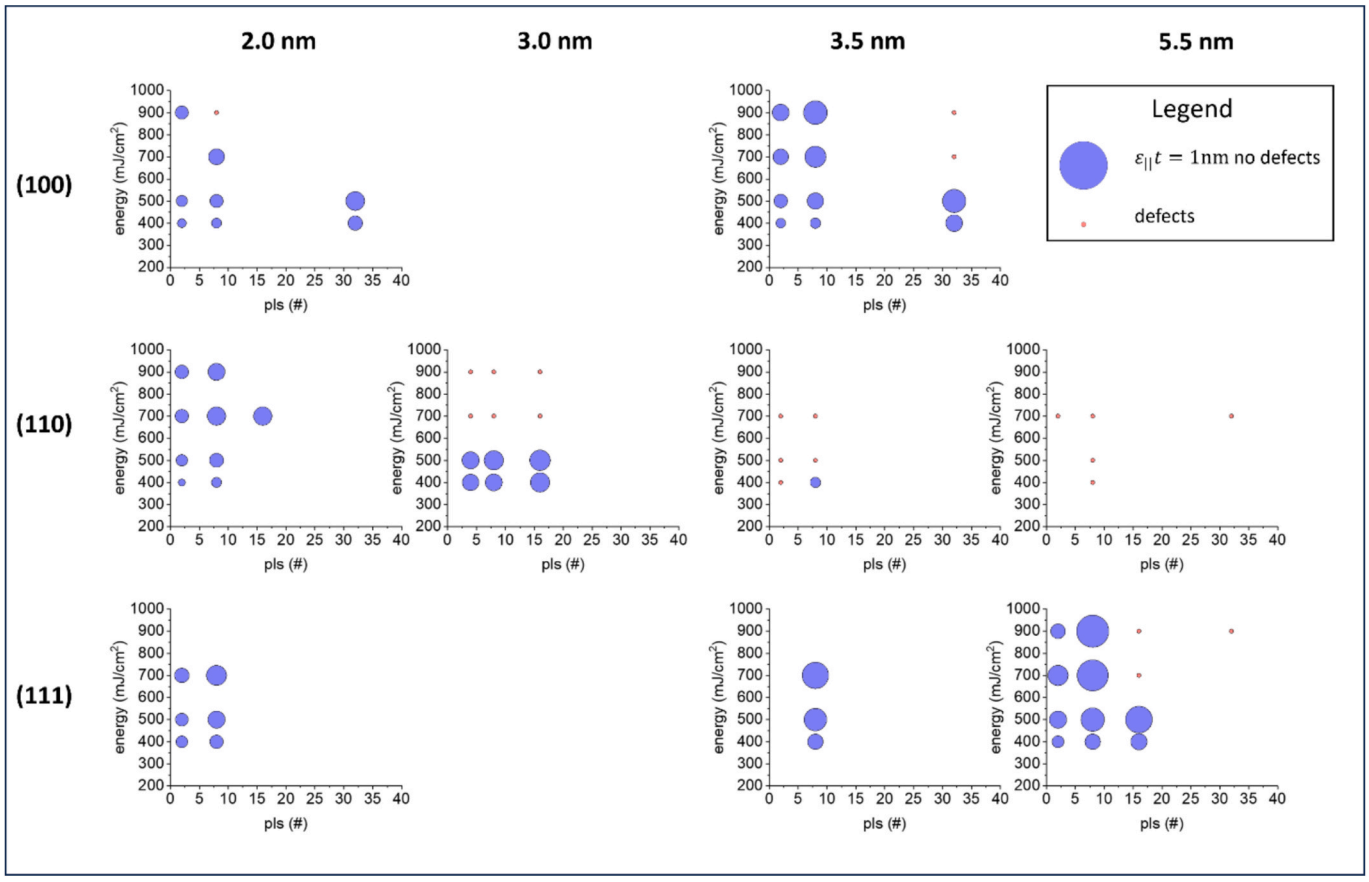

Fig. 3. Strain integral values experimentally measured through X-Ray diffraction. Each row presents the results for (100), (110), and (111) substrates respectively, while for each column, a different dose of Sb was deposited and then diffused, with values equal to 2.0, 3.0, 3.5 and 5.5 nm (7.5 10^{15}, 9.2 10^{15}, 1.15 10^{16}, 1.77 10^{16} cm^{-2}), respectively. The strain integral value of a defect-free film is proportional to the radius of the blue dot shown, while in the case of relaxed films with defects, an orange dot with a fixed radius is used. (For interpretation of the references to colour in this figure legend, the reader is referred to the web version of this article.)

maximum melt depth increases, and therefore, the system remains at high temperature for a longer time, allowing the evolution of defects (as an example, 900 mJ cm^{-2} 6 nm Ge (1 1 1), increasing the pulse number). In conclusion, it is therefore clear that the crystallographic direction that allows reaching the highest strain integral with this technique is Ge (1 1 1), achieving a value equal to 0.8 nm.

3.2. *The surface status of stressor films*

To better frame the surface/interface status before and after the film relaxation limit, we also inspected the post-PLM morphology by AFM on selected samples. Specifically, Ge (1 1 0) specimens processed with a 3 nm Sb precursor and 8 pulses were compared at low, intermediate, and high energy density in Fig. 4. At low and intermediate energy density (400 and 500 mJ cm^{-2}), the surface exhibits the shallow, pit-like texture commonly observed after nanosecond laser melting [21], with no additional long-range morphological organization. By contrast, at the highest energy density (700 mJ cm^{-2}), where HRXRD indicates the onset of strain relaxation, AFM reveals the emergence of an additional raised, network-like pattern. This correlation suggests that, once relaxation becomes active, the formation and evolution of extended defects can be coupled to the regrowth dynamics and generate a measurable morphological signature.

A plausible physical interpretation is that the rapid epitaxial regrowth following PLM becomes laterally non-uniform when interfacial defects nucleate during relaxation. These defects may propagate toward the surface during regrowth, locally perturb the solidification front, and ultimately imprint surface protrusions/undulations that form an irregular network.

Similar links between melt regime, dopant redistribution, and AFM-observed surface structuring have been reported in related laser-processing studies on group-IV alloys [70,71]. Moreover, it is well established that dislocations in germanium can act as preferential absorption centers for laser energy, facilitating localized melting and thereby modifying the solidification dynamics and the fast epitaxial regrowth [70].

Kelvin Probe Force Microscopy (KPFM) measurements (Fig. 5) were performed on the same two representative Ge (110) samples used before: the pseudomorphic (500 mJ cm^{-2}) and relaxed (700 mJ cm^{-2}) spot are now measured with this technique in another position within the same laser spot. The tip-voltage maps (not calibrated) show negligible potential modulation for the pseudomorphic sample suggesting a good lateral doping uniformity, whereas the relaxed sample exhibits a pronounced contrast that spatially correlates with the crests of the surface protrusions observed in topography. This correlation indicates that the morphological features emerging at the onset of relaxation are accompanied by a local variation in surface electronic properties and/or composition. In particular, the magnitude of the measured contrast appears larger than what would be expected from a purely doping-driven work-function shift (limited to $\sim$ half the Ge bandgap, $\approx<0.4$ eV), suggesting that compositional effects and/or charge accumulation effects, most plausibly involving surface oxides, may play a dominant role. A consistent scenario is that relaxation-related extended defects (e.g., dislocations) promote local Sb redistribution toward the surface, where exposure to ambient oxygen and/or GeOx can favor the formation of thin Sb oxides. The formation, stability, and persistence of surface

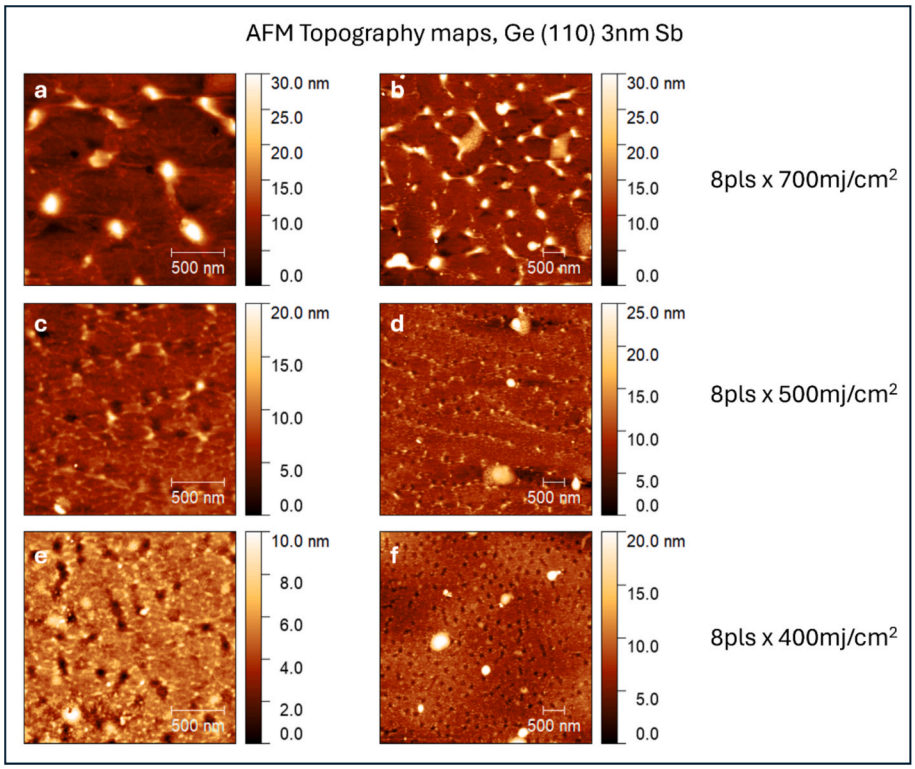

Fig. 4. AFM topography maps of PLM-treated Ge(110) samples after a 3 nm Sb deposition. From top to bottom, the topography maps refer to samples irradiated with 8 laser pulses at fluences of 700 (a,b), 500 (c,d), and 400 (e,f) mJ cm^{-2}, respectively. On the left, the topography maps show a 2 × 2 μm^2 area (a,c,e) acquired within the 5 × 5 μm^2 map on the right (b,d,f).

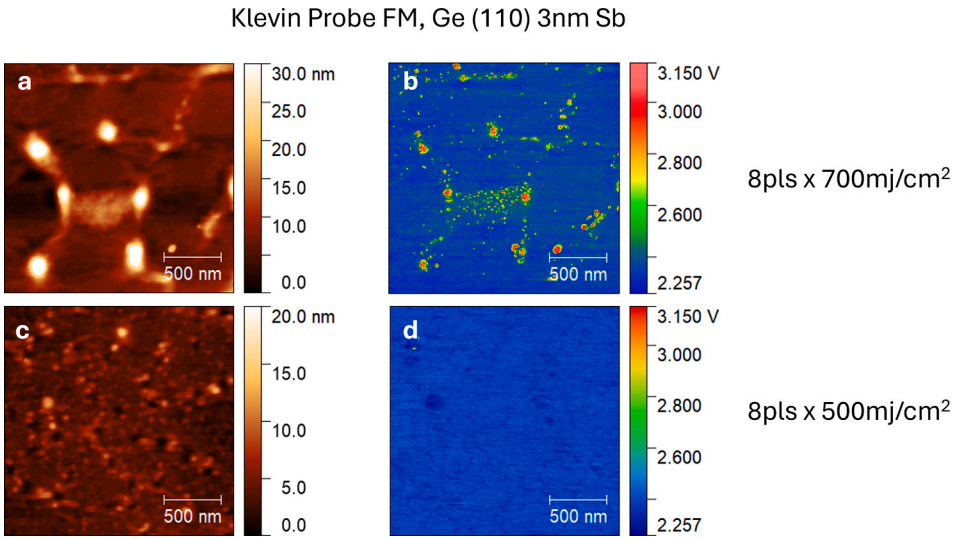

Fig. 5. KPFM maps of PLM-treated Ge (110) samples after a 3 nm Sb deposition. From top to bottom, the topography maps refer to samples irradiated with 8 laser pulses at fluences of 700 (a,b), 500 (c,d) mJ cm^{-2}, respectively. On the left, the topography maps show a 2 × 2 μm^2 area (a,c), on the right (b,d) the uncalibrated tip voltage map. (For interpretation of the references to colour in this figure legend, the reader is referred to the web version of this article.)

Sb_xO_y oxides on Ge have already been investigated by our group in the literature [34], and these results lend support to the interpretation proposed here. While the present KPFM data provide an additional surface-sensitive signature of the onset of relaxation, a definitive chemical assignment would require complementary analyses that requires more investigations that are beyond the scope of this manuscript.

3.3. Sb electrical activation

The samples synthesized so far have been electrically characterized using the Van der Pauw–Hall technique, as described in the experimental section. The analysis of electrical activation is crucial for understanding the atomic-scale behavior of the Ge:Sb alloy, especially since it is already well established that n-type dopants, and in particular Sb in Ge, contribute electronically to the strain [53]. Therefore, its direct quantification is essential to enable an accurate description of the

system.

Table 1 reports the carrier dose obtained via electrical measurements for a selection of samples. At such high Sb doses, all considered samples show partial electrical activation. As demonstrated in our earlier study [16], electrical activation in Ge:Sb obtained by PLM treatment saturates at a concentration of approximately 2.5–2.8 × 10^{20} cm^{-3} of Sb in Ge (measured on (100) orientation), which is consistently reached in our samples. In fact, even with the smallest Sb dose used (2 nm, corresponding to ~7.5 × 10^{15} cm^{-2}) and the maximum junction depth typically achieved under the laser conditions used (250–300 nm), final Sb concentrations in the range of 2.5–3.0 × 10^{20} cm^{-3} or higher can be obtained.

To provide an order-of-magnitude estimate of the Ge:Sb layer resistivity, we combine the Hall sheet carrier density n_s with an effective thickness t_{eff} (from HRXRD strain-profile simulations) and a representative electron mobility μ_e from fully analogous PLM Ge:Sb layers (see ref [16]). Assuming conduction is confined within t_{eff}, the resistivity can be estimated as $\rho \approx t_{eff}/(q\, n_s\, \mu_e)$, where q is the elementary charge. For example, using $t_{eff} = 300$ nm, $n_s = 6 \times 10^{15}$ cm^{-2}, and $\mu_e = 200$ $cm^2\ V^{-1}\ s^{-1}$ gives an extremely low resistivity of $\rho \approx 1.6 \times 10^{-4}$ Ωcm (values of the same order are obtained across the range of n_s in Table 1 and $t_{eff} \sim 100 - 500$ nm).

3.4. Sb contribution to lattice variation

Considering the data collected, it is now possible to make some quantitative considerations regarding how much antimony contributes to the dilatation of the Ge lattice cell. By defining:

$$a_{GeSb} = a_{Ge} + \Delta a_{Sb,active} x_{active} + \Delta a_{Sb,inactive} x_{inactive} \quad (4)$$

where a_{GeSb} is the cell parameter of germanium antimony alloy at a given composition, a_{Ge} is the cell parameter of germanium, and the other two terms are the contributions to the lattice parameter modification by electrically active antimony ($\Delta a_{Sbactive}$) and from the non electrically active antimony ($\Delta a_{Sbinactive}$). By considering only pseudomorphic samples, it is possible to write that $\varepsilon_{\parallel} = \frac{a_{Ge} - a_{GeSb}}{a_{GeSb}}$, which allow us to write:

$$-\varepsilon_{\parallel} \approx \frac{\Delta a_{Sbactive}}{a_{Ge}} x_{active} + \frac{\Delta a_{Sbinactive}}{a_{Ge}} x_{inactive} \quad (5)$$

By integrating the Eqs. (4) & (5) in the depth of samples, the following expression can be obtained:

$$-\int \varepsilon_{\parallel} dt = \frac{\Delta a_{active}}{a_{Ge}} \int x_{active} dt + \frac{\Delta a_{inactive}}{a_{Ge}} \int x_{inactive} dt \quad (6)$$

where t is the thickness of the considered layer. The second term of Eq. (6) is particularly interesting, as it includes quantities that can be measured using experimental techniques. For example, the integral over the thickness of the active dopant concentration corresponds exactly to the carrier dose measured through the electrical Hall effect measurement (D_{Hall}), while the second integral can be determined by subtracting the active part (just obtained from the electrical measurements) from the total amount of antimony in the layer, which is obtained from RBS measurements (D_{RBS}). The first term of the expression called integral of strain (I) is obtained from HRXRD measurements and the analysis previously described.

$$I = \frac{\Delta a_{active}}{a_{Ge}} \frac{D_{Hall}}{c_{Ge}} + \frac{\Delta a_{inactive}}{a_{Ge}} \frac{(D_{RBS} - D_{Hall})}{c_{Ge}} \quad (7)$$

where c_{Ge} is the atomic Ge concentration.

To support Eq. (7), Fig. 6 highlights the linear trend relative to the first addend using experimental data listed in Table 1.

It shows the trend of the strain integral as a function of the Hall Dose (D_{Hall}). The open circles are the measured integral of strain data that account for both active and inactive Sb atoms, while the black squares

Table 1
The most relevant values for a subset of the samples used in this study: active dopant doses measured using Van der Pauw–Hall measurements and strain integrals are reported, with the samples grouped according to the initial Sb dose and the crystallographic orientation of the germanium substrate.

Sb initial dose (cm^{-2})	Initial Sb thickness (nm) ± 0.2	Substrate orientation	PLM treatment (# of pulses × mJ cm^{-2})	Hall Active Dose D_{Hall} (cm^{-2}) ± 10%	Inactive Dose $D_{RBS} - D_{Hall}$ (cm^{-2}) ± 3%	Strain integral modulus I (nm) ± 0.05 nm
7.5 10^{15}	2.0	(100)	8 × 400	2.4 10^{15}	5.1 10^{15}	0.25
			2 × 500	3.1 10^{15}	4.4 10^{15}	0.28
			8 × 500	3.9 10^{15}	3.6 10^{15}	0.33
			32 × 500	5.1 10^{15}	2.4 10^{15}	0.47
			2 × 900	4.2 10^{15}	3.3 10^{15}	0.33
1.15 10^{16}	3.5	(100)	8 × 400	1.9 10^{15}	9.6 10^{15}	0.26
			2 × 500	3.4 10^{15}	8.1 10^{15}	0.34
			8 × 500	4.0 10^{15}	7.5 10^{15}	0.41
			32 × 500	6.1 10^{15}	5.4 10^{15}	0.58
			2 × 900	4.6 10^{15}	6.9 10^{15}	0.42
7.5 10^{15}	2.0	(110)	8 × 400	2.5 10^{15}	5.0 10^{15}	0.25
			2 × 500	3.1 10^{15}	4.4 10^{15}	0.29
			8 × 500	3.9 10^{15}	3.6 10^{15}	0.35
			2 × 700	5.2 10^{15}	2.3 10^{15}	0.34
			2 × 900	3.8 10^{15}	3.7 10^{15}	0.33
7.5 10^{15}	2.0	(111)	8 × 400	3.9 10^{15}	3.6 10^{15}	0.34
			2 × 500	3.7 10^{15}	3.8 10^{15}	0.32
			8 × 500	4.5 10^{15}	3.0 10^{15}	0.43
			2 × 700	4.1 10^{15}	3.4 10^{15}	0.37
1.77 10^{16}	5.5	(111)	8 × 500	2.5 10^{15}	1.52 10^{16}	0.59
			16 × 500	2.5 10^{15}	1.52 10^{16}	0.67
			2 × 700	2.7 10^{15}	1.50 10^{16}	0.51
			8 × 700	–	–	0.79
			2 × 900	4.5 10^{15}	1.32 10^{16}	0.37
			8 × 900	9.4 10^{15}	8.3 10^{15}	0.80

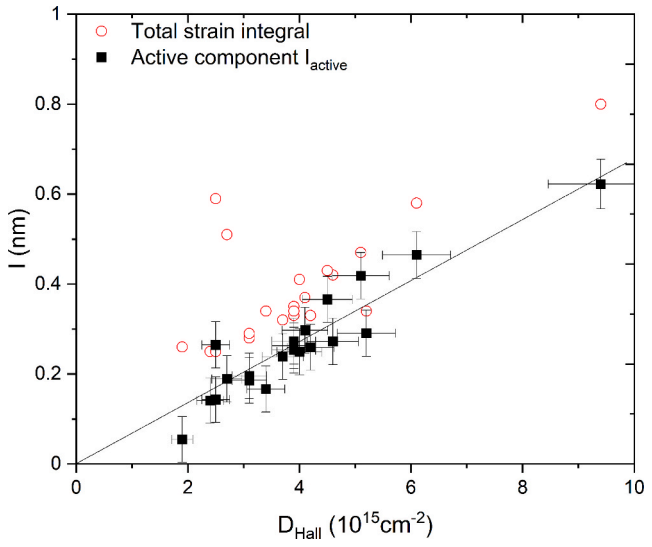

Fig. 6. Experimental values of the strain integral component as a function of the Hall dose (i.e. D_{Hall}, the electrically active component). Open circles denote the integral of the total strain $I = -\int \varepsilon_{\parallel} dt$, whereas black squares denote only the component arising from the active dopant. Black line is the linear fitting of the black square data. Error bars are shown for the active-component data. The error bars for the open circles have the same horizontal values and slightly smaller vertical uncertainties, and are not shown to avoid overcrowding of the plot. (For interpretation of the references to colour in this figure legend, the reader is referred to the web version of this article.)

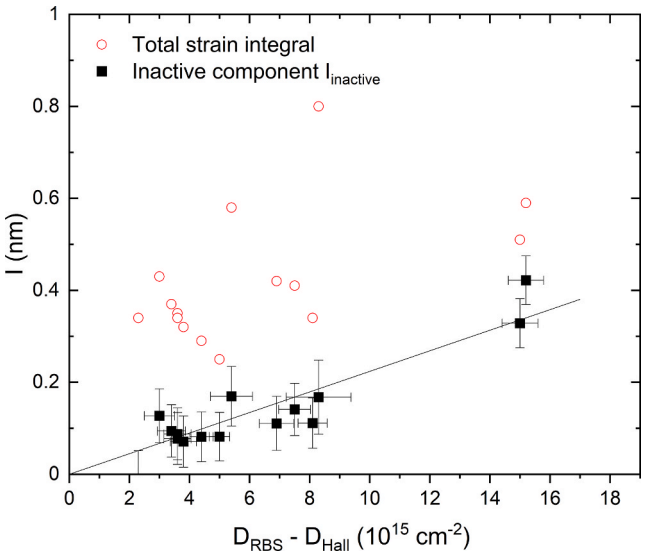

Fig. 7. Experimental values of the strain integral component as a function of the inactive dose (i.e. D_{RBS}-D_{Hall}). Open circles denote the integral of the total strain $I = -\int \varepsilon_{\parallel} dt$, whereas black squares denote only the component arising from the inactive dopant. Black line is the linear fitting of the black square data. Error bars are shown for the inactive-component data. The error bars for the open circles have the same horizontal values and slightly smaller vertical uncertainties and are not shown to avoid overcrowding of the plot. (For interpretation of the references to colour in this figure legend, the reader is referred to the web version of this article.)

are the portion of the integral of strain due to the electrically active Sb atoms. These values are obtained by subtracting the inactive contribution from the total strain integral, i.e. by plotting $I_{active} = I - \Delta a_{inactive}(D_{RBS} - D_{Hall}) a_{Ge}^{-1} c_{Ge}^{-1}$. As can be seen in Fig. 6, the total integral of strain does not show a clear relationship with the Hall dose, while the black square data (related only to the active component of I) exhibits a linear behavior, supporting the linearity relationship expressed in Eqs. (6) and (7). In other words, by subtracting from the measured total strain integral the component due to the electrically inactive contribution, the data show a linear trend with the Hall dose.

A similar trend can also be observed for the inactive component as a function of the inactive dose ($D_{RBS} - D_{Hall}$): Fig. 7 shows a linear trend also in this case justifying the second part of Eq. (7) ($I_{inactive} = I - \Delta a_{active}(D_{Hall}) a_{Ge}^{-1} c_{Ge}^{-1}$).

Thanks to the relationship expressed by Eq. (7), it is now possible to obtain the Δa_{active} and $\Delta a_{inactive}$ values from experimental data by using a multiparametric fitting, where the active dose and inactive dose are the variables. The obtained values are: $\Delta a_{Sb,active}$ is equal to 1.7 ± 0.1 Å and $\Delta a_{Sb,inactive}$ 0.5 ± 0.1 Å.

These values can be compared with other results reported in the literature. A first relevant comparison can be made with the work by Xu et al. [54]. In their study, the β parameter (defined as $\Delta a/a = \beta N_i$ where N_i is a shallow substitutional donor in Ge on Si (001)) was calculated from experimental data where Sb dopant reaches lower concentration compared to this work and is reported to be fully substitutional and electrically active. Converting this value into a $\Delta a_{Sb,active}$ yields 1.9 Å, which, within the experimental uncertainties of both studies, results in two compatible outcomes.

Another useful comparison involves the germanium–tin system, which exhibits lattice expansion without electronic contributions, using an atom with an atomic number similar to that of Sb. This system was previously investigated by our research group [21], leading to an estimated Δa_{Sn} of 0.8 Å, significantly lower than in the Ge:Sb system. This confirms the advantageous choice of using Sb as a dopant impurity to induce maximum strain, as it appears to be the most effective option among candidates for pulsed laser melting, given equal concentration levels.

Quantifying the strain contribution of electrically inactive Sb is, to our knowledge, a novel result. Notably, this contribution is comparable to that of Sn, indicating that free-carrier–induced lattice expansion more than doubles the purely steric expansion expected from atomic size alone.

3.5. Sb lattice localization

To investigate what happens in the crystal lattice with high concentrations of inactive dopant, a Ge (1 0 0) sample deposited with 8.5 nm of Sb and PLM treated with 4pls at 500 mJ cm^{-2} has been chosen for lattice localization analysis. Initial electrical characterization by van der Pauw Hall-effect measurements shows that only 1.3 10^{15} cm^{-2} of the total 2.98 10^{16} cm^{-2} antimony dose is electrically active in the selected sample. This corresponds to an activation fraction of roughly 4–5%, meaning that the remaining 2.85 10^{16} cm^{-2} is electrically inactive.

The simplest structural hypothesis for this system is that the inactive dopant is arranged in a disordered configuration within the lattice, i.e. it does not preferentially occupy any specific germanium lattice site. To test this hypothesis, lattice-location measurements were carried out using ion beams, performing angular scans with collimated beams as described in the Experimental section. RBS angular scans were recorded along the ⟨001⟩ and ⟨111⟩ crystallographic axes of the Ge (1 0 0) substrate and Fig. 8 show the results. The transition from axial to random alignment for the impurity is shown in red, while for the host atoms are shown in blue in panels a, b. In addition to the experimental data, Fig. 8a and b shows the expected angular-scan signal if Sb were completely randomly distributed in the lattice with a green dotted line. Under a fully random distribution, the Sb yield should be independent of the tilt angle for scans around both the ⟨001⟩ and ⟨111⟩ axes, presenting a constant χ value equal to 1. By contrast, the electrically active component, assumed to be substitutional, should follow the germanium angular dependence, exhibiting a channeling dip equal to that of Ge matrix. Given the measured electrical activation, roughly 95% of the Sb is electrically

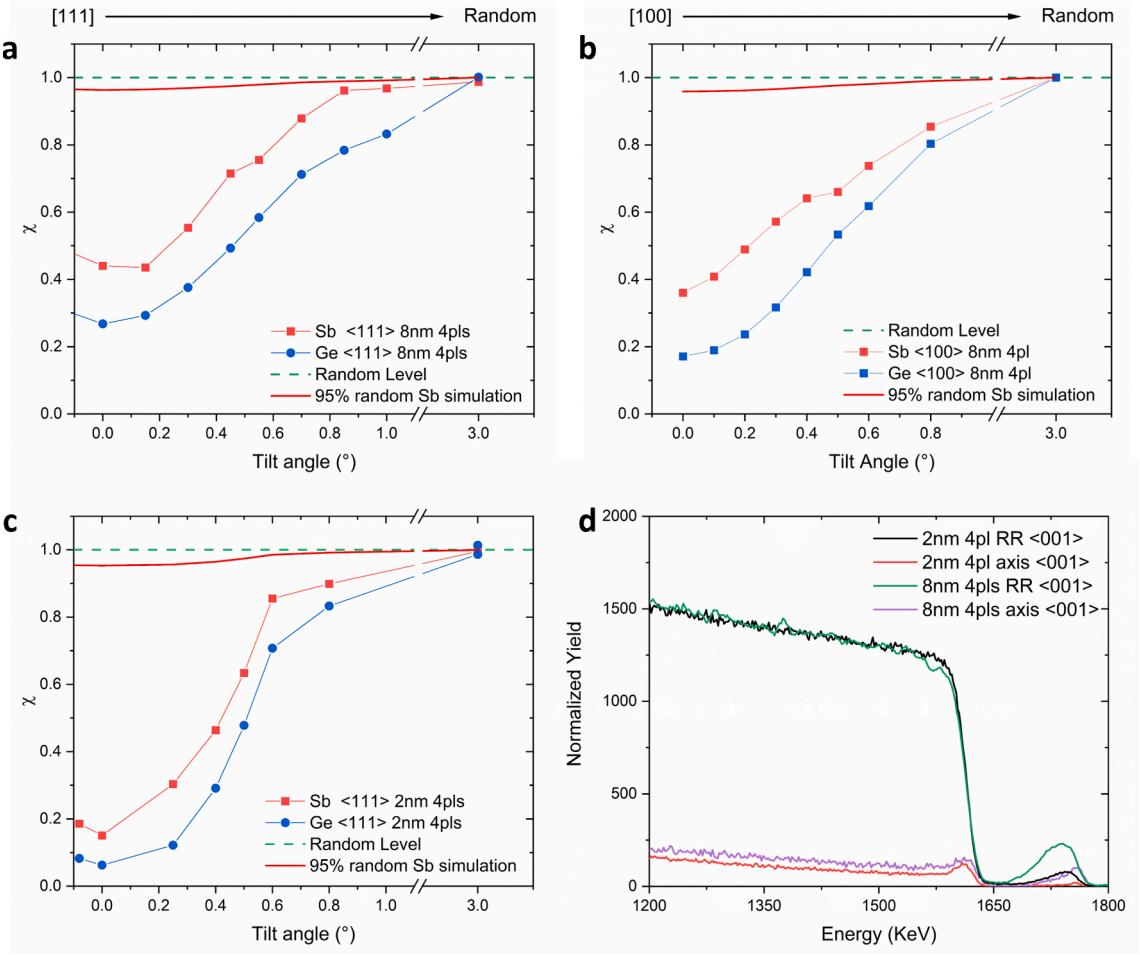

Fig. 8. Channeling angular scan of PLM diffused Sb in Ge (100) samples measured along <111> axis for 8 nm 4pls sample (**a**), <001> axis for 8 nm 4pls sample (**b**). The laser treatments were performed at 500 mJ cm^{-2}. Red points are referred to the backscattering yield of Sb signal as a function of the tilt angle, while blue points are referred to Ge signal. The angular scan starts in a perfect axial alignment (axis <111> or <001>, tilt angle = 0°) and it ends in a non-aligned condition (also called random condition). These yields are obtained by integrating the entire RBS Sb peak zone and an equivalent Ge zone. The continuous red lines are a simulation of angular scans in the case of 95% of Sb atoms are randomly distributed in the matrix and 5% in substitutional sites (see in the text). (For interpretation of the references to colour in this figure legend, the reader is referred to the web version of this article.)

inactive and only about 5% should produce an angle-dependent signal with a minimum comparable to Ge. The red continuous curve in Fig. 6(a and b) is therefore the weighted sum of these two contributions.

The experimental data clearly contradicts this hypothesis: for both scan directions, the Sb signal displays an angular trend similar to the Ge atoms one, indicating a distribution different from a random one. This suggests that a substantial fraction of Sb atoms is crystallographically aligned with the lattice, rather than being randomly distributed. Indeed, the angular scans around both the ⟨001⟩ and ⟨111⟩ axes exhibit essentially the same behavior, confirming that Sb occupies substitutional and/or nearly substitutional lattice sites.

A closer inspection of the data shows that the shape of the channeling dip is consistent with a small displacement plus a substitutional configuration of Sb, in which part of the dopant is substitutional and the remainder occupies sites slightly displaced from substitutional positions. In agreement with the literature [72], this distribution is characterized by a "knee" on the Sb signal shoulders of the dip arising from the superposition of a purely substitutional signal and a small-displacement component. This feature is visible in the 8 nm sample, where a clear change in the Sb yield appears between 0.4° and 0.6° as the scan transitions toward the random level for both the ⟨111⟩ and ⟨001⟩ directions.

Disclosing the presence of slightly off-sites atoms, some hypotheses on the nature of the effect are advanced. In general, the formation of donor-vacancies complexes could lead to the trapping of charge within the cluster, thus preventing that a donor atom donates an electron [73] and could be compatible with a small displacement lattice position [74], according to the cluster structure. Some works in the literature have studied the formation of Sb clusters in Ge [73–75], verifying the formation energy and the stability of Sb_nV_m clusters via ab-inito DFT studies. Coutinho et al. [75] calculated that a certain amounts of small Sb_nV_m clusters present small formation energies (<1 eV) and in particular Sb_2V cluster exhibit a 0.52 eV formation energy, with an atom arrangement that is compatible with the data presented in this work. It is therefore likely that the analyzed material contains this type of cluster, which would explain both the electrical activation and the lattice-site localization measurements.

Concerning stability, donor–vacancy aggregates in Ge are expected to be relatively robust at moderate thermal budgets. Ab-initio calculations indicate that Sb_2V has a well-defined ground-state structure and low formation energy (0.52 eV), with binding energies in the ~1–2.4 eV range depending on the reaction pathway, implying a strong driving force for vacancy–donor aggregation 75. Reported annealing data for irradiation-induced vacancy-related traps in Sb-doped Ge indicate stability of SbV-related levels up to ~170 °C and divacancies up to ~250 °C, with some hole traps persisting up to ~300 °C. Therefore, while these complexes can explain the coexistence of lattice-aligned Sb with low electrical activation, elevated-temperature processing steps and/or high irradiation fluence could, in principle, promote defect

reactions and modify the electrical compensation state. No dedicated post-annealing campaign was performed in this work; samples were characterized in the as-processed state after the nanosecond PLM melt/regrowth cycle carried out at room temperature.

3.6. Direct Ge bending measurements

A direct measurement of the curvature of thin Ge samples induced by a Ge:Sb stressor layer was carried out using a profilometer. Two types of 8×9 mm^2 samples with thicknesses ranging from 150 to 180 μm were fully deposited and treated using the PLM technique for this purpose. Based on the findings of the previous study, both Ge (110) samples with 2 nm of Sb (treated with 500 mJ cm^{-2}, 8 pulses and 700 mJ cm^{-2}, 8 pulses) and Ge (111) samples (700 mJ cm^{-2}, 8 pulses) were tested.

As reported in Table 1 and Fig. 3, these treatments result in strain integrals of 0.35 nm and 0.46 nm for the Ge (110) samples, respectively, while the Ge (111) sample is expected to exhibit the maximum strain integral, i.e., 0.8 nm.

The results of these measurements are shown in Fig. 9. The curvature radius, obtained through direct profilometer measurements, is reported for the different tested samples as a function of the laser treatment conditions. Specifically, on the left graph, the two measurements on the Ge (110) samples along two orthogonal directions are shown in black and red, respectively, to highlight the two resulting curvatures.

The experimental values can be compared with an estimated curvature derived from Stoney's equation Eq. (2) and strain integral measured by HRXRD. This estimate predicts the same curvature in the two orthogonal directions and can be applied only to the case of no strain relaxation, since in case of film relaxation we cannot have the strain integral evaluation.

The agreement between the curvature radius estimate with the two methods is good, thereby validating this experimental approach. The same analysis was carried out on a Ge (111) sample, using the treatment that produced the highest strain integral. The results are shown in the graph with star-shaped markers. As predicted by the estimation, a curvature radius of approximately 4.5 m was measured.

It is worth noting that the curvature radius obtained in (110) and (111) samples with a 6 nm 700 mJ cm^{-2} 8 pulses surface layer is very different mainly since strain relaxation occurs only in the first of the two samples. Moreover, we notice that the curvature for the relaxed sample is asymmetric in the two orthogonal directions. As we said, this is not predicted by the Stoney formula, and we can intuitively say that even if the elastic constants of Ge are not symmetric both layer and film have the same constants in the two directions causing the same curvature. This difference could be due to asymmetry in the relaxation mechanism, which was already observed in other epitaxial systems [76]. On the other hand, asymmetry is not present for pseudomorphic samples (2 nm 500 mJ cm^{-2} 8 pulses and 700 mJ cm^{-2} 8 pulses).

These results are highly promising for the development of crystalline Ge-based devices where controlled bending is required. One notable example is *Crystalline Light Sources*, which are currently of great interest for the generation of high-brilliance, ultra-high-energy (>1 MeV) photon beams.

Indeed, the ability to deposit Sb and selectively process regions of a crystal using PLM, enabled through standard lithography techniques, makes it feasible to fabricate periodically bent crystals with periods on the order of tens to hundreds of microns.

Thanks to the findings of this work, it is now possible to identify the most suitable process parameters and crystallographic orientations, as well as to quantitatively assess the achievable bending, thus paving the way for the practical implementation of such advanced devices.

Further confirmation of the estimates obtained through profilometry comes from an X-Ray topography measurement using synchrotron light. In particular, the Ge (110) sample with a 2 nm Sb deposit and treated with PLM at 700 mJ cm^{-2} for 8 pulses was measured with a 10.5 keV beam using the symmetric 220 reflection of germanium, as described in the dedicated section. Thanks to this effect, the crystal curvature has been estimated to be 14 m. This value is compatible with the direct bending measurement obtained with the profilometer (see Fig. 9) and further supports the carried-out analyses.

4. Conclusion

In this work, we have demonstrated that the sputter deposition of thin Sb layers on Ge, followed by pulsed laser melting (PLM), is an effective strategy to induce extremely high levels of strain in germanium.

Thanks to the non-equilibrium nature of the PLM technique, Sb was incorporated into Ge well beyond its equilibrium solid solubility limit (which is 1.2 10^{19} cm^{-3} [66,77]). We established the maximum incorporation levels of Sb in Ge for the formation of pseudomorphic layers on various crystallographic orientations. Significant differences were observed among the different substrate orientations, and a rationale based on the recrystallization dynamics during the melt-solidification process has been proposed to explain these findings.

Regarding the electrical activation of antimony, the activation levels achieved are comparable to the record values previously reported by our group [16]. However, this work extends the analysis to different

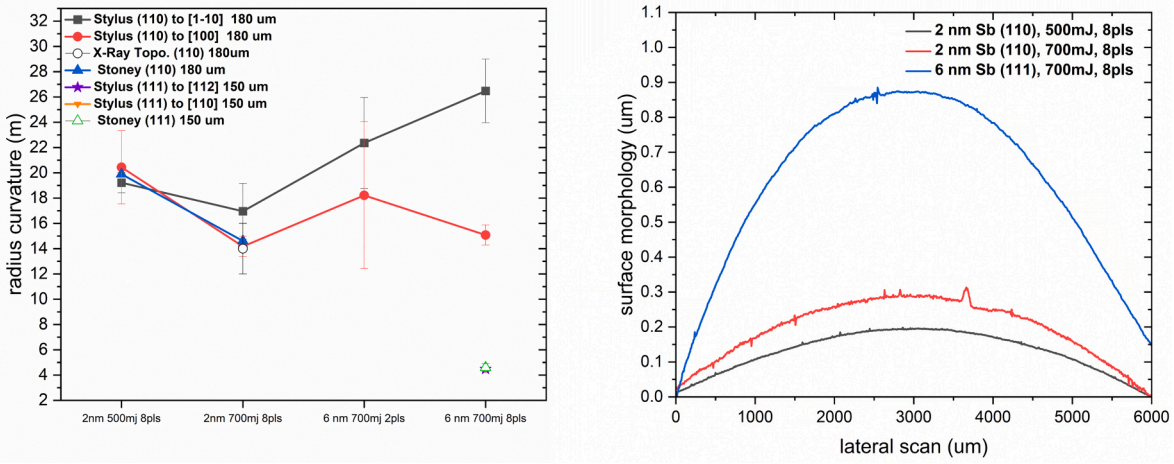

Fig. 9. Curvature radius measurements of various thin samples, obtained through direct profilometer measurements of sample bending. The comparison between the experimental curvature radii and the expected values is shown in the left-hand graph, while the right-hand graph displays examples of direct curvature profiles measured with the profilometer.

crystallographic orientations of Ge showing different behavior with the used Ge orientation. The contribution of Sb to lattice expansion was extracted from diffraction data, showing a Δa_{Sb} value of approximately 1.7 Å for the active dopants, substantially higher than the 0.8 Å associated with Sn [21]. This not only confirms previously reported values obtained at lower concentration regimes but also allows for a clear separation between the electrically active and inactive contributions to lattice expansion. We determined that non active Sb still gives a lattice expansion with a linear coefficient equal to 0.5 Å similar to the results of non-doping Sn species.

From the combined analysis of diffraction and electrical activation data, the Ge (111) orientation emerged as the most promising for inducing maximum bending. Relaxation phenomena occur only under more extreme conditions, allowing strain integrals up to 0.8 nm while maintaining the alloy pseudomorphic to the substrate.

To experimentally validate this result, direct bending measurements were performed on specially designed thin Ge samples. These tests confirmed that a single stressor layer can produce curvature radii as low as 4.5 m, in good agreement with estimates based on Stoney's equation and strain integral measurements, paving the way for the construction of devices such as crystalline undulators, of utmost importance for the production of high-brilliance crystalline gamma-ray sources [13,37,78].

CRediT authorship contribution statement

Francesco Sgarbossa: Writing – original draft, Methodology, Investigation, Formal analysis, Conceptualization. **Davide Valzani:** Software, Investigation, Formal analysis, Data curation. **Filippo Nicolasi:** Investigation, Data curation. **Gianluigi Maggioni:** Writing – review & editing, Methodology, Investigation. **Chiara Carraro:** Investigation. **Marco Romagnoni:** Investigation. **Thu Nhi Tran Caliste:** Validation, Software, Methodology. **John P. Sutter:** Investigation. **Enrico Napolitani:** Validation, Supervision, Funding acquisition. **Davide De Salvador:** Writing – review & editing, Supervision, Resources, Project administration, Funding acquisition.

Declaration of competing interest

The authors declare the following financial interests/personal relationships which may be considered as potential competing interests: Davide De Salvador reports financial support was provided by European Union. Davide De Salvador reports financial support was provided by National Institute of Nuclear Physics. Enrico Napolitani reports financial support was provided by University of Padua. Francesco Sgarbossa reports financial support was provided by Diamond Light Source Ltd. If there are other authors, they declare that they have no known competing financial interests or personal relationships that could have appeared to influence the work reported in this paper.

Acknowledgements

This project has received funding from the European Union under the agreement 101046458 named TECHNO-CLS horizon EIC 2021 pathfinder project [78].

This work was partially supported by Istituto Nazionale di Fisica Nucleare (INFN) under the national BOND project granted from V national commission and from the University of Padova research infrastructure project SENSITISE for the Pulsed Laser Melting infrastructure.

This work received financial support from the Diamond Light Source synchrotron under proposal number OM36299-1 and OM34545-1 at beamline B16.

The authors are grateful for the technical support provided by Nicola Argiolas and Luca Bacci. The authors also thank Dr. Enrico Di Russo for his support with the AFM.

Data availability

Data will be made available on request.

References

[1] J. Eberth, J. Simpson, From Ge(Li) detectors to gamma-ray tracking arrays-50 years of gamma spectroscopy with germanium detectors, Prog. Part. Nucl. Phys. 60 (2008) 283–337.
[2] G. Maggioni, et al., Pulsed laser diffusion of thin hole-barrier contacts in high purity germanium for gamma radiation detectors, Eur. Phys. J. A 54 (2018).
[3] S. Bertoldo, et al., Lithium-free hyperpure germanium detectors with enhanced thickness, area, and segmentation via pulsed laser melting, Mater. Sci. Semicond. Process. 200 (2025) 109967.
[4] S. Gupta, B. Magyari-Köpe, Y. Nishi, K.C. Saraswat, Achieving direct band gap in germanium through integration of Sn alloying and external strain, J. Appl. Phys. 113 (2013).
[5] H.H. Gandhi, et al., Gold-hyperdoped germanium with room-temperature sub-band-gap optoelectronic response, Phys. Rev. Appl 14 (2020).
[6] M. El Kurdi, et al., Control of direct band gap emission of bulk germanium by mechanical tensile strain, Appl. Phys. Lett. 96 (2010) 94–97.
[7] T.K.P. Luong, V. Le Thanh, A. Ghrib, E.K. Moustafa, P. Boucaud, Making germanium, an indirect band gap semiconductor, suitable for light-emitting devices, Adv. Nat. Sci. Nanosci. Nanotechnol. 6 (2015) 2–7.
[8] S.R. Cherry, J.A. Sorenson, M.E. Phelps, Physics in nuclear medicine, Soc. Nuclear Med. (2013).
[9] R. Pillarisetty, Academic and industry research progress in germanium nanodevices, Nature 479 (2011) 324–328.
[10] C. Boztug, J.R. Sánchez-Pérez, F. Cavallo, M.G. Lagally, R. Paiella, Strained-germanium nanostructures for infrared photonics, ACS Nano 8 (2014) 3136–3151.
[11] M. Romagnoni, et al., Bent crystal design and characterization for high-energy physics experiments, Crystals (Basel). 12 (2022) 1–28.
[12] M. Romagnoni, et al., The GALORE project, Eur. Phys. J. D 76 (2022).
[13] A.V. Korol, A.V. Solov, Crystal-based intensive gamma-ray light sources, Eur. Phys. J. D 74 (2020).
[14] D.S. Davide, et al., Metodo per ottenere un cristallo piegato periodicamente, cristallo ottenuto con tale metodo e dispositivo per la produzione di radiazione elettromagnetica comprendente tale cristallo, (2024).
[15] S. Bertoldo, et al., New method for the production of thin and stable , segmented n + contacts in HPGe detector, Eur. Phys. J. A 57 (2021) 1–10.
[16] C. Carraro, et al., N-type heavy doping with ultralow resistivity in Ge by Sb deposition and pulsed laser melting, Appl. Surf. Sci. 509 (2020) 145229.
[17] M. El Kurdi, G. Fishman, Ś. Sauvage, P. Boucaud, Band structure and optical gain of tensile-strained germanium based on a 30 band kp formalism, J. Appl. Phys. 107 (2010).
[18] J. Frigerio, et al., Optical properties of highly n-doped germanium obtained by in situ doping and laser annealing, J. Phys. D Appl. Phys. 50 (2017).
[19] J.R. Sánchez-Pérez, et al., Direct-bandgap light-emitting germanium in tensilely strained nanomembranes, Proc. Natl. Acad. Sci. USA 108 (2011) 18893–18898.
[20] D. Fontana, et al., Ex-situ N-type heavy doping of Ge1-Xsnx epilayers by surface Sb deposition and pulsed laser melting, Appl. Surf. Sci. 600 (2022).
[21] E. Di Russo, et al., Synthesis of relaxed Ge0.9Sn0.1/Ge by nanosecond pulsed laser melting, Appl. Surf. Sci. 612 (2023).
[22] K.P. Homewood, M.A. Lourenço, The rise of the GeSn laser, Nat. Photonics 9 (2015) 78–79.
[23] D. Stange, et al., GeSn/SiGeSn heterostructure and multi quantum well lasers, ACS Photonics 5 (2018) 4628–4636.
[24] J. Frigerio, et al., Tunability of the dielectric function of heavily doped germanium thin films for mid-infrared plasmonics, Phys. Rev. B 94 (2016) 1–18.
[25] L.A. Terrazos, et al., Theory of hole-spin qubits in strained germanium quantum dots, Phys. Rev. B 103 (2021).
[26] N.W. Hendrickx, et al., A four-qubit germanium quantum processor, Nature 591 (2021).
[27] G. Scappucci, et al., The germanium quantum information route, Nat. Rev. Mater., 6 (2021) 926–943, Preprint at Doi: 10.1038/s41578-020-00262-z.
[28] W. Scandale, et al., First results on the SPS beam collimation with bent crystals, Phys. Lett. Sec. B: Nucl. Element. Particle High-Energy Phys. 692 (2010) 78–82.
[29] L. Bandiera, et al., Investigation of radiation emitted by sub GeV electrons in oriented scintillator crystals, Nucl. Instrum. Methods Phys. Res. A 1060 (2024) 169022.
[30] L. Bandiera, et al., Strong reduction of the effective radiation length in an axially oriented scintillator crystal, Phys. Rev. Lett. 121 (2018) 21603.
[31] L. Bandiera, et al., Investigation on radiation generated by sub-GeV electrons in ultrashort silicon and germanium bent crystals, Eur. Phys. J. C 81 (2021).
[32] L. Bandiera, et al., Crystal-based pair production for a lepton collider positron source, Eur. Phys. J.C 123 (2022) 1–13.
[33] M. Romagnoni, et al., Crystal fabrication techniques for enhanced performance in planar channeling, Nucl. Instrum. Methods Phys. Res. A 1082 (2026).
[34] F. Sgarbossa, et al., Self-limiting Sb monolayer as a diffusion source for Ge doping, Appl. Surf. Sci. 496 (2019) 8–9.
[35] F. Sgarbossa, Germanium monolayer doping: successes and challenges for the next generation Ge devices, Mater. Sci. Semicond. Process. 167 (2023) 107795.
[36] A. Mazzolari, et al., Silicon crystals for steering high-intensity particle beams at ultrahigh-energy accelerators, Phys. Rev. Res. 3 (2021).

[37] A. Korol, A.V. Solov'yov, Novel lights sources beyond free electron lasers, (2022), https://link.springer.com/bookseries/5267.
[38] H. Backe, et al., Observation of narrow-band gamma radiation from a boron-doped diamond superlattice with an 855 MeV electron beam, (2025), http://arxiv.org/abs/2504.17988.
[39] A.V. Korol, W. Greiner, Channeling of positrons through periodically bent crystals: on the fesability of crystalline undulator and gamma-laser, Int. J. Modern Phys. E 13 (2004) 867–916.
[40] A.V. Korol, A.V. Solov, W. Greiner, Photon emission by an ultra-relativistic particle channeling in a periodically bent crystal, (2001).
[41] V.V. Haurylavets, V.K. Ivanov, A.V. Korol, A.V. Solov'yov, Atomistic modelling of electron propagation and radiation emission in oriented bent ultra-thin Si and Ge crystals, Nucl. Instrum. Methods Phys. Res. A 1058 (2024).
[42] L. Malagutti, et al., From simulation to fabrication: Realizing silicon crystalline undulators with silicon nitride stressor layer patterning, Nucl. Instrum. Methods Phys. Res. A 1076 (2025).
[43] R. Camattari, et al., Silicon crystalline undulator prototypes: Manufacturing and X-ray characterization, Phys. Rev. Accel. Beams 22 (2019) 44701.
[44] V. Guidi, L. Lanzoni, A. Mazzolari, G. Martinelli, A. Tralli, Design of a crystalline undulator based on patterning by tensile Si 3N4 strips on a Si crystal, Appl. Phys. Lett. 90 (2007) 3–5.
[45] D.D. Salvador, et al., Innovative remotely-controlled bending device for thin silicon and germanium crystals, J. Instrum. 13 (2018) C04006.
[46] S. Carturan, et al., Germanium strips for channeling: Study of the crystal quality after slicing and chemical etching, Mater. Chem. Phys. 132 (2012) 641–651.
[47] V.M. Biryukov, et al., Accelerator tests of crystal undulators. Advanced Photon Sources and Their Application, 2004.
[48] L. Lanzoni, A. Mazzolari, V. Guidi, A. Tralli, G. Martinelli, On the mechanical behaviour of a crystalline undulator, Int. J. Eng. Sci. 46 (2008) 917–928.
[49] A.V. Korol, A.V. Solov'yov, W. Greiner, Channeling and radiation in periodically bent crystals, 69 (2013).
[50] G.B. Sushko, A.V. Korol, A.V. Solov'Yov, Intensive γ -ray light sources based on oriented single crystals, Phys. Rev. Accel. Beams 27 (2024).
[51] K. Toko, et al., Progress and perspectives on polycrystalline germanium thin films: advances in solid-phase crystallization. Appl. Phys. Rev., 12 (2025), Preprint at Doi: 10.1063/5.0229016.
[52] C. Carraro, Hyperdoping of germanium by pulsed laser melting, University of Padova, 2020.
[53] C. Xu, C.L. Senaratne, P. Sims, J. Kouvetakis, J. Menéndez, Ultralow resistivity Ge:Sb heterostructures on Si using hydride epitaxy of deuterated stibine and trigermane, ACS Appl. Mater. Interfaces 8 (2016) 23810–23819.
[54] C. Xu, C.L. Senaratne, J. Kouvetakis, J. Men, Experimental doping dependence of the lattice parameter in n -type Ge: IDENTIFYING the correct theoretical framework by comparison with Si, Phys. Rev. B 041201 (2016) 1–5.
[55] F. Cerdeira, M. Cardona, Effect of carrier concentration on the raman frequencies of Si and Ge, Phys. Rev. B 5 (1972) 1440–1454.
[56] G.G. Stoney, The tension of metallic films deposited by electrolysis. Proc. Royal Soc. London, 82, 172–175 (1090).
[57] G.C.A.M. Janssen, M.M. Abdalla, F. van Keulen, B.R. Pujada, B. van Venrooy, Celebrating the 100th anniversary of the Stoney equation for film stress: developments from polycrystalline steel strips to single crystal silicon wafers, Thin Solid Films 517 (2009) 1858–1867, https://doi.org/10.1016/j.tsf.2008.07.014.
[58] G. Maggioni, et al., Diffusion doping of germanium by sputtered antimony sources, Mater. Sci. Semicond. Process. 75 (2018) 118–123.
[59] J. Poate, J.W. Mayer, Laser annealing of semiconductors, Elsevier, 1982.
[60] C. Fuccio, A. La Magna, Laser annealing process in semiconductor techology, Elsevier, 2021.
[61] R. Duffy, E. Napolitani, F. Cristiano, Materials science issues related to the fabrication of highly doped junctions by laser annealing of Group IV semiconductors, in: Laser Annealing Processes in Semiconductor Technology: Theory, Modeling and Applications in Nanoelectronics, Elsevier, 2021, pp. 175–250, https://doi.org/10.1016/B978-0-12-820255-5.00007-6.
[62] V. Boldrini, et al., Optimal process parameters for phosphorus spin-on-doping of germanium, Appl. Surf. Sci. 392 (2016) 1173–1180.
[63] E. Bagli, et al., Enhancement of the inelastic nuclear interaction rate in crystals via antichanneling, Phys. Rev. Lett. 123 (2019) 044801.
[64] T.N.T. Thi, et al., Synchrotron Bragg diffraction imaging characterization of synthetic diamond crystals for optical and electronic power device applications, J. Appl. Crystallogr. 50 (2017) 561–569.
[65] J.P. Sutter, V. Dhamgaye, O. Fox, K. Sawhney, The diamond light source program for crystal inspection using X-ray topography, J. Phys.: Conf. Ser. 3010 (2025). Institute of Physics.
[66] M. Oehme, J. Werner, E. Kasper, Molecular beam epitaxy of highly antimony doped germanium on silicon, J. Cryst. Growth 310 (2008) 4531–4534.
[67] S. Ndiaye, et al., Atom probe tomography of hyper-doped Ge layers synthesized by Sb in-diffusion by pulsed laser melting, Mater. Sci. Semicond. Process. 164 (2023) 1–8.
[68] J.Z. Tischler, B.C. Larson, D.M. Mills, Time-resolved x-ray study of Ge during pulsed laser melting, Appl. Phys. Lett. 52 (1988) 1785–1787.
[69] S. Brotzmann, H. Bracht, Intrinsic and extrinsic diffusion of phosphorus, arsenic, and antimony in germanium, J. Appl. Phys. 103 (2008) 033508.
[70] V.Y. Zheleznov, et al., Effect of nanosecond ultraviolet laser pulses on the surface of germanium single crystals, Russ. Microelectron. 52 (2023) 741–749.
[71] M. Frauenrath, et al., Nanosecond laser annealing of pseudomorphic GeSn layers: impact of Sn content, Mater. Sci. Semicond. Process. 163 (2023).
[72] J.R. Tesmer, M. Nastasi, Handbook of modern ion beam materials analysis, Material Research Society, 1995.
[73] A. Chroneos, Dopant-vacancy cluster formation in germanium, J. Appl. Phys. 107 (2010) 7–10.
[74] A. Satta, et al., Atomistic simulation of ion channeling in heavily doped Si:As, Nucl. Instrum. Methods Phys. Res. B 230 (2005) 112–117.
[75] J. Coutinho, et al., Early stage donor-vacancy clusters in germanium, J. Mater. Sci. Mater. Electron. 18 (2007) 769–773.
[76] M. Natali, F. Romanato, E. Napolitani, D. De Salvador, A.V. Drigo, Lattice curvature generation in graded InxGa1-xAs/GaAs buffer layers, Phys. Rev. B 62 (2000) 11054.
[77] C. Claeys, E. Simoen, Germanium-based technologies: from materials to devices, Germanium-Based Technol.: Materials to Devices 1–449 (2007), https://doi.org/10.1016/B978-0-08-044953-1.X5000-5.
[78] https://mbnresearch.com/TECHNO-CLS/Main. Emerging technologies for crystal-based gamma-ray light sources (Techno CLS), (2022). EIC Pathfinder Project Preprint at Doi: 10.3030/101046458.